sustainability

MDPI

Article

Adaptive Risk-Budgeted Rolling Dispatch for Service Continuity in Integrated Electricity–Gas–Heat Systems

Jiaxi Kang, Tong Qian and Wenhu Tang *

School of Electric Power Engineering, South China University of Technology, Guangzhou 510641, China; epjx.kang@mail.scut.edu.cn (J.K.); qiantong@scut.edu.cn (T.Q.)
* Correspondence: wenhutang@scut.edu.cn

Abstract

Integrated electricity–gas–heat systems underpin sustainable energy provision by coupling renewable, gas, and thermal resources across carriers. Sustainable operation of such systems must limit service loss caused by cross-carrier contingencies while maintaining economic efficiency and tracking carbon performance. This paper develops a 6 h rolling linear dispatch framework in which a security-margin floor, a scenario-weighted unserved-energy limit, and a conditional value-at-risk (CVaR) limit jointly define the admissible operating domain. The two risk limits adapt to the evolving load, forecast uncertainty, and gas-supply state, and future forecasts use only the error observed at the current dispatch instant. Across 30 paired forecast-error realizations, the adaptive method reduces the weighted unserved-energy index and the maximum hourly CVaR by 4.88% and 4.38%, respectively, relative to a fixed-cap rolling method under identical inputs, at a 2.14% cost increase. The equal-mean-budget comparison shows that temporal allocation adds a smaller, operationally modest improvement, with a paired CVaR difference of −0.094 MWh (95% CI: −0.108 to −0.079 MWh). A transfer case on the linear IEEE 39-bus–Belgian 20-node–DHS 6-node model keeps the network flexibility equivalent within its calibrated 0–65 MW domain, and all three rolling schedules pass 24 h full-topology linear routing checks without additional shedding at nominal capacities. These results establish implementability within the tested linear models; all reported risk indices are comparative scenario-risk measures rather than annual reliability statistics. By jointly safeguarding service continuity, economic efficiency, and carbon performance, the proposed framework supports the environmental, economic, and social dimensions of sustainable integrated-energy operation.

Keywords: integrated energy systems; service continuity; risk-budget allocation; conditional value-at-risk; receding-horizon dispatch; cross-carrier contingencies

Check for updates

Academic Editors: Cong Zhang, Wei Zhang, Zipeng Liang and Shibo Chen

Received: 3 August 2026
Revised: 19 August 2026
Accepted: 1 September 2026
Published: 2 September 2026

Copyright: © 2026 by the authors. Licensee MDPI, Basel, Switzerland. This article is an open access article distributed under the terms and conditions of the Creative Commons Attribution (CC BY) license.

1. Introduction

Integrated electricity–gas–heat systems coordinate electricity networks, natural gas infrastructure, district heating networks, renewable generation, conversion devices, energy storage, and flexible demand. Such coordination provides additional operating flexibility through energy substitution and complementary resource utilization across different carriers. However, it also creates new pathways through which disturbances can propagate among interconnected energy subsystems. For example, a gas-source or pipeline outage may restrict fuel delivery to gas-fired generators and combined heat and power (CHP) units, simultaneously reducing electricity and heat production. Conversely, an electricity-network restriction may limit electric-boiler operation and increase the heat-production

burden on fuel-consuming units. Therefore, sustainable and resilient operation requires not only nominal energy balance and equipment feasibility but also explicit control of the service losses caused by cross-carrier contingency propagation. Coordinated multi-energy operation should therefore balance economic efficiency and continuity of electricity, gas, and heating services under stressed conditions. Carbon output is monitored as a secondary operating indicator.

These requirements align with the three pillars of sustainable energy development. Environmentally, coordinated operation of coupled energy carriers improves the utilization of renewable and low-carbon resources and limits carbon-intensive backup generation. Economically, coordinated corrective operation across carriers can avoid excessive, unconditional over-conservatism, obtaining service-continuity guarantees at a modest and state-dependent cost. Socially, limiting unserved energy under cross-carrier contingencies protects the continuity and resilience of electricity, gas, and heating services on which households, businesses, and critical infrastructure depend. The present study therefore contributes to the sustainable development goals of affordable and clean energy (SDG 7), sustainable cities and communities (SDG 11), and climate action (SDG 13) [1].

Integrated-energy-system modeling has developed from compact energy-hub and multi-energy-carrier optimal-flow formulations [2,3] toward explicit representations of electricity–heat interactions, CHP units, electric boilers, renewable generation, and combined cooling, heating, and power systems [4,5]. Network-coupled studies have further demonstrated that gas deliverability, power-to-gas conversion, heat transport, and infrastructure interdependence can materially affect both operating feasibility and service continuity [6–12]. Stochastic, interval, and hybrid stochastic–robust formulations have also been proposed to represent uncertainty in electricity–heat systems and energy hubs [13,14], whereas coordinated electricity–gas optimization and security-constrained gas-flow models show that gas-network restrictions can directly alter power-system dispatch feasibility [15–17]. These studies establish the physical basis for coordinated multi-energy operation, but physical coupling constraints alone do not directly limit the distribution of post-contingency consequences. Recent reviews further distinguish secure multi-energy operation from the broader preparedness–response–recovery process normally associated with resilience [18,19].

Security-constrained unit commitment and economic dispatch provide the principal operational frameworks for enforcing network and contingency feasibility. Existing studies have incorporated volatile renewable generation, adaptive uncertainty sets, and natural gas transmission constraints into security-constrained scheduling [20–22]. These methods determine whether a schedule remains feasible under specified operating conditions or contingencies and accordingly allocate generation and reserve resources. Nevertheless, deterministic security criteria primarily distinguish feasible operating states from infeasible ones. A schedule satisfying a prescribed security-margin threshold may still be exposed to considerable expected energy not supplied or severe losses under a small number of high-consequence contingencies. Deterministic feasibility alone therefore cannot fully characterize the magnitude or distribution of post-contingency consequences.

Reliability assessment complements deterministic security analysis by characterizing service continuity using indices such as expected demand not supplied [23]. Resilience and infrastructure-interdependency studies further emphasize that failures should be evaluated in terms of both their likelihood and their consequences and that disturbances may propagate across coupled infrastructures [11,12,24,25]. However, contingency consequences are frequently calculated after an operating schedule has been obtained. Although such ex-post assessments can identify vulnerable components or rank severe contingencies, they do not directly change the set of admissible dispatch decisions. Consequently, a schedule

associated with excessive average or tail losses may remain economically optimal if the risk indicators are not embedded in the scheduling model. This creates an assessment–decision gap between identifying system risk and controlling that risk through operational decisions.

This gap is particularly important when a small number of gas-source, pipeline, or coupling-device outages dominates the upper tail of the loss distribution. Scheduling a gas source according only to its nominal production limit, for example, may produce an apparently balanced solution that cannot be delivered through the associated pipeline path. Moreover, post-contingency loss is commonly treated either as an ex-post performance indicator or as a weighted term in the objective function. A weighted objective permits cost and risk to compensate for each other according to a predetermined coefficient, whereas system operators may instead require explicit upper limits on acceptable expected and tail losses. A constraint-based formulation is therefore needed to identify which schedules become inadmissible as physical-security, expected-loss, and tail-loss requirements are progressively imposed.

Conditional value-at-risk (CVaR) provides a coherent measure of tail loss and admits a tractable optimization representation [26–28]. It has subsequently been incorporated into risk-aware stochastic and real-time energy dispatch, including coordinated electricity–gas operation [29]. Chance-constrained and distributionally robust optimization provide alternative frameworks for controlling uncertainty when probability distributions are known only partially or estimated from data [30–35]. Recent studies have extended CVaR and distributionally robust formulations to integrated-energy planning and coordinated electricity–gas–heat energy and reserve scheduling [36,37]. Unlike these approaches, the present study does not construct a distributional ambiguity set. Instead, it embeds the average and tail consequences of screened contingencies directly into the dispatch feasible set. Scenario-weighted expected loss represents the average consequence across screened contingencies, while CVaR controls the concentration of loss in the upper tail. Because the case-study weights are derived from consequence screening rather than independently observed outage frequencies, the resulting indicators are interpreted as comparative scenario-risk measures rather than annual reliability statistics.

Risk limits must also respond to changing operating conditions. Rolling- or receding-horizon optimization provides a practical mechanism for incorporating updated forecasts and system states into operational decisions. Model predictive control for microgrids, rolling dispatch for energy hubs, multi-timescale integrated-energy scheduling, and stochastic rolling-horizon planning have demonstrated the value of repeatedly updating short-horizon decisions as new information becomes available [38–41]. However, the reviewed studies generally update forecasts and operating schedules, while explicit adaptation of expected-loss and CVaR limits to evolving load, forecast uncertainty, and gas-supply stress remains insufficiently examined. Fixed risk limits may be unnecessarily conservative under normal conditions but insufficiently restrictive during stressed periods. In practice, the first failure mode can procure reserve or conversion capacity that adds cost without commensurate risk reduction, whereas the second can preserve a nominally acceptable cap even as peak load, forecast error, or gas stress increases the consequences of the same contingency. This motivates an adaptive risk-budget mechanism that links acceptable contingency consequences to the evolving system state.

An additional issue concerns the economic interpretation of risk control. In a convex dispatch model, the dual multiplier of a binding constraint measures the local sensitivity of the optimal objective value to a marginal relaxation of that constraint [42–44]. For a risk constraint, however, this shadow sensitivity is not equivalent to the cost of deploying an actual reserve, demand-response, or conversion resource. The former represents an infinitesimal change in the constraint boundary, whereas the latter reflects a finite and phys-

ically feasible resource adjustment. Conflating these quantities may lead to an unjustified market-price interpretation. They should therefore be evaluated separately as a risk-limit shadow sensitivity and an incremental risk-mitigation cost.

The preceding review identifies three related gaps. First, deterministic security criteria and ex-post risk assessment do not share a unified feasible-domain representation that separately controls physical feasibility, security margin, average contingency consequence, and tail consequence. Second, risk-aware dispatch models generally use fixed risk limits and do not adapt the admissible risk level to updated operating conditions. Third, aggregate multi-energy schedules may overestimate corrective flexibility when locational deliverability of gas and conversion resources is not checked. Addressing these gaps requires a framework that embeds risk indicators directly in the rolling-dispatch feasible set while retaining tractability for repeated operational use.

Accordingly, this study develops a security–risk feasible-domain and CVaR-aware rolling-dispatch framework for integrated electricity–gas–heat systems. In this paper, cross-carrier flexibility refers to dispatchable actions—including CHP adjustment, electric-boiler conversion, demand response, and locational gas redispatch—that modify the balance of at least two energy carriers. The contributions are as follows:

1. A nested security–risk feasible domain is established by successively imposing physical constraints, a security-margin requirement, a scenario-weighted expected-loss limit, and a CVaR limit. Unlike a weighted risk term in the objective function, this formulation explicitly excludes schedules that violate prescribed average- or tail-risk limits.
2. An adaptive CVaR-aware rolling-dispatch model is developed. A 6 h rolling linear program re-establishes the security–risk feasible domain from the updated load, forecast uncertainty, and gas-supply state. A fitted affine contingency-loss representation, supplemented by the 95th percentile of held-out underprediction errors, limits optimistic loss estimates while preserving linear tractability.
3. Economic cost, the scenario-weighted unserved-energy index, weighted tail risk, security margin, carbon output, and network deliverability are evaluated separately. The framework is further applied to an interface-equivalent IEEE 39-bus–Belgian 20-node–DHS 6-node dispatch model, followed by a post-dispatch full-topology linear consistency check that verifies the schedules against the linear capacity limits of the coupled network model.

Figure 1 summarizes the evidence chain from the updated information state to executable rolling decisions and the subsequent verification steps.

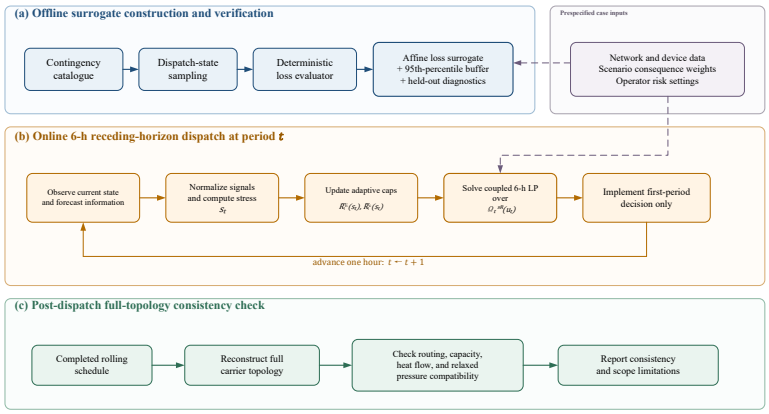

Figure 1. Overall workflow of the proposed rolling security–risk dispatch, including state updates, adaptive risk-limit construction, optimization, implementation, and the separate surrogate and network checks.

The remainder of this paper is organized as follows. Section 2 defines the security–risk feasible domain and presents the CVaR-aware rolling-dispatch model. Section 3 describes the case systems, contingency interface, compared methods, and reproducibility setup. Section 4 reports and discusses the numerical results, sensitivity tests, network-transfer checks, computational performance, and limitations. Section 5 concludes the paper.

2. Materials and Methods

2.1. Problem Setting and Risk Metrics

Let $t \in \mathcal{T} = \{1, \ldots, N_T\}$ denote a dispatch period and $z \in \mathcal{Z} = \{1, \ldots, N_Z\}$ a screened contingency. The local decision vector x_t contains conventional and gas-fired generation, CHP electric and heat output, electric-boiler consumption, reserve, demand response, and other cross-carrier corrective actions. The information state u_t contains the latest load and renewable forecasts, forecast-error level, gas-supply stress, equivalent-model residual, and equipment-availability information. Intertemporal constraints are introduced separately in Section 2.5.

The post-contingency unserved-energy consequence associated with (x_t, u_t, z) is denoted by $L_{z,t}(x_t, u_t) \geq 0$. Let w_z be a normalized scenario weight:

$$w_z \geq 0, \qquad \sum_{z \in \mathcal{Z}} w_z = 1. \tag{1}$$

In the case study, these weights are obtained by normalizing consequence- screening scores rather than independently observed outage frequencies. Accordingly, all quantities defined below are comparative scenario-risk indices and should not be interpreted as annual reliability statistics.

The scenario-weighted unserved-energy index (WUEI) is

$$R_t^E(x_t, u_t) = \sum_{z \in \mathcal{Z}} w_z L_{z,t}(x_t, u_t). \tag{2}$$

For confidence level $\alpha \in (0, 1)$, the corresponding scenario-weighted CVaR index is

$$R_t^C(x_t, u_t) = \min_{\eta_t} \left\{ \eta_t + \frac{1}{1-\alpha} \sum_{z \in \mathcal{Z}} w_z \left[L_{z,t}(x_t, u_t) - \eta_t \right]_+ \right\}. \tag{3}$$

For the macro-equivalent dispatch model, define the normalized peak-load indicator

$$\pi_t = \max\left\{0, \frac{P_t^L - 775}{240}\right\}. \tag{4}$$

The security margin used by all macro-model comparisons is

$$M_t^{\text{mac}} = 0.245 - 0.105\pi_t - 0.64\sigma_t - 0.23s_t^g + 0.0014r_t + 0.0018d_t + 0.0022f_t, \tag{5}$$

where P_t^L is forecast electric demand, σ_t is the normalized forecast-uncertainty indicator, s_t^g is the normalized gas-stress indicator, and r_t, d_t, f_t are reserve, demand response, and cross-carrier corrective capacity, respectively. This margin is a pre-specified normalized case-study security index, not an outage probability or an N–1 stability margin. Its coefficients were fixed before the method comparison by three transparent construction rules: adverse state variables receive negative signs, corrective resources receive positive signs, and coefficient magnitudes make their contributions comparable over the stated case-study

ranges while retaining a feasible and active margin constraint. Table 1 reports the complete macro construction; no coefficients were fitted to the reported dispatch outcomes.

Table 1. Construction of the macro security-margin index.

Term	Case-Study Range	Coefficient	Signed Contribution Range
Intercept	–	0.245	0.245
Peak indicator π_t	0–0.85	−0.105	−0.089–0
Uncertainty σ_t	0–0.12	−0.640	−0.077–0
Gas stress s_t^g	0–0.30	−0.230	−0.069–0
Reserve r_t (MW)	10–95	0.0014	0.014–0.133
Demand response d_t (MW)	0–30	0.0018	0–0.054
Cross-carrier flexibility f_t (MW)	0–65	0.0022	0–0.143

The network-transfer case retains a separate location-aware margin:

$$\begin{aligned} M_t^{\text{net}} = {} & 0.205 - 0.105\pi_t - 0.64\sigma_t - 0.23s_t^g + 0.0014r_t + 0.0018d_t \\ & + 0.00018\left(p_{1,t}^{GG} + p_{2,t}^{GG}\right) + 0.00035p_t^{CHP} + 0.00020h_t^{CHP} + 0.0016h_t^{EB}. \end{aligned} \tag{6}$$

Equation (6) retains the same adverse-state coefficients. Its corrective-resource terms replace the aggregate cross-carrier term with location-aware gas-fired, CHP, and electric-boiler actions over their source-case bounds. The corresponding maximum positive contributions are approximately 0.219 for combined gas-fired output, 0.091 for CHP power, 0.078 for CHP heat, and 0.080 for electric-boiler heat. The lower intercept compensates for this more detailed resource decomposition. The one-at-a-time ±20% coefficient test in Section 4.3 evaluates whether conclusions depend on these case-study choices. The appropriate expression is denoted generically by $M_t(x_t, u_t)$ below. A larger value represents a safer state. The required floor is $\underline{M}_t$, and the upper limits on Equations (2) and (3) are $\overline{R}_t^E$ and $\overline{R}_t^C$, respectively.

2.2. Security–Risk Feasible Domain

For a fixed information state u_t, the local physical feasible domain is

$$\Omega_t^P(u_t) = \{x_t \mid g_t(x_t, u_t) = 0,\ h_t(x_t, u_t) \le 0\}, \tag{7}$$

where g_t contains the electricity, gas, and heat balance equations and h_t contains the within-period device, reserve, demand-response, network, and conversion limits. Ramping and other state-transition constraints are included in the horizon-level feasible set defined later.

The security, expected-risk, and final security–risk feasible domains are

$$\Omega_t^S(u_t) = \left\{x_t \in \Omega_t^P(u_t) \mid M_t(x_t, u_t) \ge \underline{M}_t\right\}, \tag{8}$$

$$\Omega_t^E(u_t) = \left\{x_t \in \Omega_t^S(u_t) \mid R_t^E(x_t, u_t) \le \overline{R}_t^E\right\}, \tag{9}$$

$$\Omega_t^{SR}(u_t) = \left\{x_t \in \Omega_t^E(u_t) \mid R_t^C(x_t, u_t) \le \overline{R}_t^C\right\}. \tag{10}$$

These sets satisfy

$$\Omega_t^{SR}(u_t) \subseteq \Omega_t^E(u_t) \subseteq \Omega_t^S(u_t) \subseteq \Omega_t^P(u_t). \tag{11}$$

Unlike a weighted risk penalty, this construction excludes a schedule that violates a prescribed limit rather than retaining it at a higher objective value. Economic dispatch searches over Ω_t^P, security-constrained dispatch over Ω_t^S, expected-risk dispatch over Ω_t^E, and the proposed formulation over Ω_t^{SR}. Figure 2 illustrates these nested feasible domains.

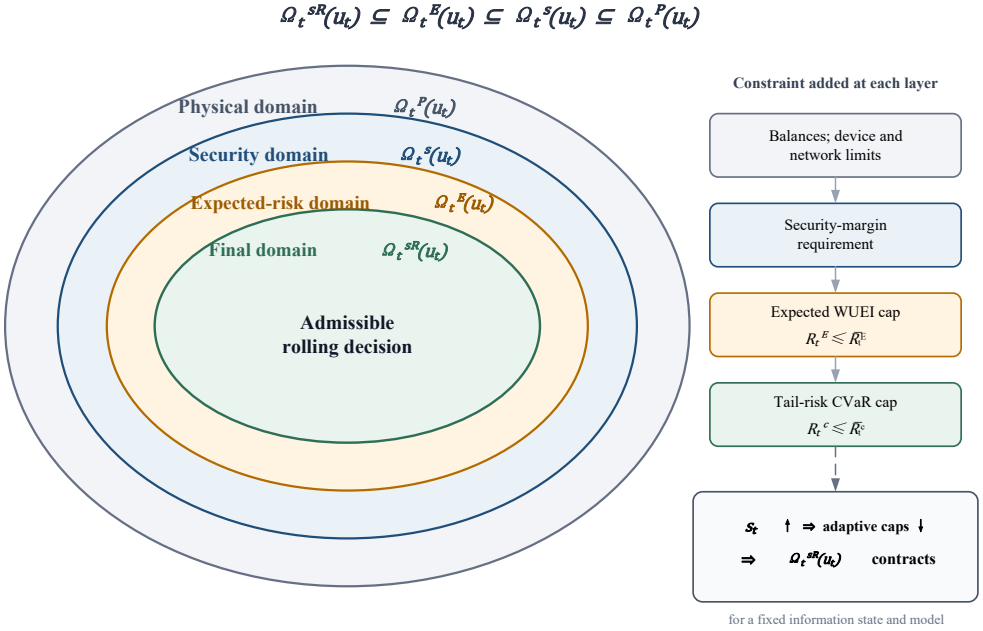

Figure 2. Nested physical, security, expected-risk, and final security–risk feasible domains. Higher operating stress tightens the adaptive risk caps and can shrink the innermost admissible domain.

Property 1 (monotonicity under limit tightening). *For fixed u_t, let $\overline{R}_t^{E\prime} \leq \overline{R}_t^{E}$, $\overline{R}_t^{C\prime} \leq \overline{R}_t^{C}$, and $\underline{M}_t' \geq \underline{M}_t$. If both domains are nonempty, then*

$$\Omega_t^{SR}\left(u_t; \overline{R}_t^{E\prime}, \overline{R}_t^{C\prime}, \underline{M}_t'\right) \subseteq \Omega_t^{SR}\left(u_t; \overline{R}_t^{E}, \overline{R}_t^{C}, \underline{M}_t\right), \tag{12}$$

and the minimum dispatch cost over the tightened domain cannot be lower than that over the original domain. This follows directly from set inclusion and is used only to interpret the cost–risk sensitivity results.

2.3. Quantile-Buffered Affine Loss Representation

To retain a linear dispatch problem, the screened-contingency evaluator is approximated over the sampled dispatch region. The fitted consequence for contingency z and period t is

$$\widehat{L}_{z,t}(r_t, d_t, f_t; u_t) = \ell_{z,t}^0(u_t) - \beta_{z,t}^r r_t - \beta_{z,t}^d d_t - \beta_{z,t}^f f_t, \tag{13}$$

where $\ell_{z,t}^0(u_t)$ is the state-dependent intercept and r_t, d_t, f_t denote reserve, demand response, and cross-carrier corrective capacity. Nonnegative least squares imposes

$$\ell_{z,t}^0,\ \beta_{z,t}^r,\ \beta_{z,t}^d,\ \beta_{z,t}^f \geq 0. \tag{14}$$

The positive held-out underprediction error is

$$e_{z,j}^+ = \max\left\{L_{z,j}^{\mathrm{ref}} - \max\{0, \widehat{L}_{z,j}\}, 0\right\}, \tag{15}$$

where j indexes held-out samples pooled across the 24 h for contingency z. The base contingency-specific buffer is

$$\epsilon_z^{95} = Q_{0.95}\left(e_{z,j}^+\right). \tag{16}$$

The fitted coefficients and buffers are calibrated under the nominal profile. For an updated information state, the implementation rescales them using

$$q_{z,t}(u_t) = \frac{\ell_{z,t}^{0,\mathrm{ana}}(u_t)}{\max\{\ell_{z,t}^{0,\mathrm{ana}}(u_t^{\mathrm{nom}}), 10^{-9}\}}, \tag{17}$$

where $\ell_{z,t}^{0,\mathrm{ana}}$ is the intercept of the analytic screened-loss evaluator. Hence, the operational coefficients and buffer are

$$\left(\ell_{z,t}^{0}, \beta_{z,t}^{r}, \beta_{z,t}^{d}, \beta_{z,t}^{f}, \epsilon_{z,t}\right) = q_{z,t}\left(\ell_{z,t}^{0,\mathrm{fit}}, \beta_{z,t}^{r,\mathrm{fit}}, \beta_{z,t}^{d,\mathrm{fit}}, \beta_{z,t}^{f,\mathrm{fit}}, \epsilon_{z}^{95}\right). \tag{18}$$

The loss variable used by the optimizer represents

$$L_{z,t} = \max\{0, \widehat{L}_{z,t}\} + \epsilon_{z,t}. \tag{19}$$

It is implemented without binary variables through

$$L_{z,t} \geq \widehat{L}_{z,t} + \epsilon_{z,t}, \tag{20}$$

$$L_{z,t} \geq \epsilon_{z,t}. \tag{21}$$

Because $L_{z,t}$ is bounded above through the risk constraints, the optimizer selects its smallest feasible value. Equations (20) and (21) therefore give the required epigraph representation.

At each of the 24 h, 96 dispatch states are sampled with $r_t \sim U[10, 95]$ MW, $d_t \sim U[0, 30]$ MW, and $f_t \sim U[0, 65]$ MW using a fixed random seed whose value is reported in the reproducibility package. Each state is evaluated under four screened contingencies, producing 9216 observations. Complete dispatch states, rather than individual contingency rows, are assigned to the training and held-out subsets to prevent the same state from appearing in both. The reference values $L_{z,t}^{\mathrm{ref}}$ are generated by the deterministic screened-contingency evaluator used to construct the case study.

The aggregate held-out MAE and RMSE are 0.228 and 0.639 MWh, respectively. The simple mean of the four contingency-specific buffers is 0.706 MWh, whereas the consequence-weighted expected-loss buffer is 1.701 MWh and the nominal CVaR buffer is 2.297 MWh. These statistics measure agreement with the reference evaluator only. In particular, the quantile buffer reduces observed underprediction on the held-out sample but does not provide a distribution-free coverage guarantee for unseen operating states.

Table 2 and Figure 3 disaggregate the held-out results by contingency. Each row contains 678 held-out samples. C1 and C2 dominate the absolute error because their consequence scales are much larger than those of C3 and C4. Adding the contingency-specific 95th-percentile positive-error buffer reduces the observed held-out underprediction frequency from 38.05–42.33% to 5.01% for every contingency.

Table 2. Per-contingency held-out error of the fitted affine loss surrogate.

Contingency	MAE (MWh)	RMSE (MWh)	95th-Percentile Buffer (MWh)	Underprediction Before (%)	Underprediction After (%)
C1	0.700	1.216	2.297	42.33	5.01
C2	0.199	0.397	0.494	40.27	5.01
C3	0.005	0.011	0.012	38.05	5.01
C4	0.008	0.015	0.020	41.00	5.01

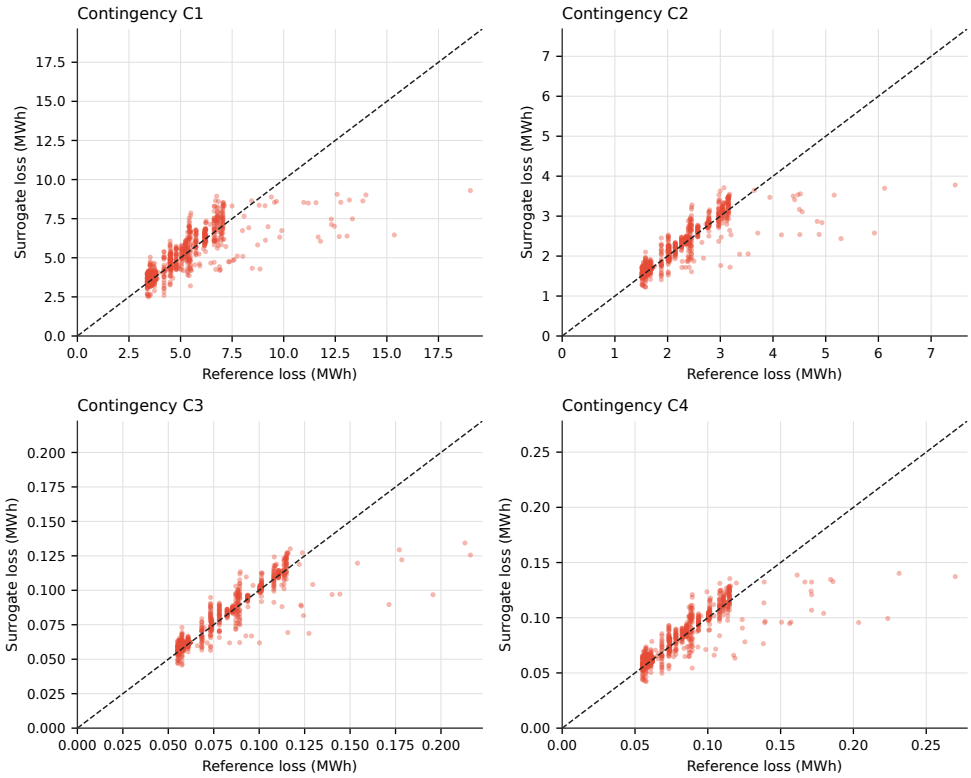

Figure 3. Direct held-out comparison between the fitted affine surrogate and the deterministic reference evaluator for each screened contingency. The dashed line is equality; the points are shown before adding the underprediction buffer.

Because the same held-out subset determines each empirical quantile and the reported post-buffer frequency, the 5.01% values are descriptive calibration diagnostics rather than independent coverage estimates. External validation would require an independently sampled or physically higher-fidelity evaluator.

For the CVaR epigraph, auxiliary variables $s_{z,t}$ satisfy

$$s_{z,t} \geq L_{z,t} - \eta_t, \tag{22}$$

$$s_{z,t} \geq 0, \qquad \forall z \in \mathcal{Z}. \tag{23}$$

The CVaR limit is

$$\eta_t + \frac{1}{1-\alpha} \sum_{z \in \mathcal{Z}} w_z s_{z,t} \leq \overline{R}_t^C. \tag{24}$$

With continuous dispatch variables, the fitted affine representation and Equations (20)–(24) preserve linearity. Binary commitment or discrete corrective actions would instead yield a mixed-integer linear program.

2.4. Integrated Electricity–Gas–Heat Constraints

The network model instantiates Ω_t^P on the selected electricity, gas, and district-heating interfaces. Let $\mathbf{A}_e$, $\mathbf{A}_g$, and $\mathbf{A}_h$ be node–branch incidence matrices. A positive incidence entry denotes flow into a node, and a negative entry denotes flow out of a node.

The dispatch LP retains five electrical interface nodes (buses 24, 30, 33, 37, and 39). Its electric balance and capacity constraints are

$$\mathbf{A}_e \mathbf{f}_t^e + \mathbf{p}_t^{CG} + \mathbf{p}_t^{GG} + \mathbf{p}_t^{CHP} + \mathbf{p}_t^{RES} - \mathbf{p}_t^L + \mathbf{p}_t^{DR} - \mathbf{p}_t^{EB} = \mathbf{0}, \tag{25}$$

$$-\overline{\mathbf{f}}^e \leq \mathbf{f}_t^e \leq \overline{\mathbf{f}}^e. \tag{26}$$

Here, $\mathbf{p}_t^{EB}$ is electric-boiler consumption and the other positive terms are nodal injections. The five flow variables form a capacity-limited transport representation; they are not susceptance–angle DC line flows. A separate post-dispatch check reconstructs the complete IEEE 39-bus linear DC balance and angle equations from the scheduled generation totals.

For the Belgian20 gas network,

$$\begin{aligned}\mathbf{A}_g\mathbf{f}_t^g + \mathbf{g}_t^{GW} - \mathbf{\Gamma}^{GG}\left(\boldsymbol{\gamma}^{GG} \odot \mathbf{p}_t^{GG}\right) \\ - \mathbf{\Gamma}^{CHP}\left(\boldsymbol{\gamma}_P^{CHP} \odot \mathbf{p}_t^{CHP} + \boldsymbol{\gamma}_H^{CHP} \odot \mathbf{h}_t^{CHP}\right) - \mathbf{d}_t^g = \mathbf{0},\end{aligned} \tag{27}$$

$$-\overline{\mathbf{f}}^g \le \mathbf{f}_t^g \le \overline{\mathbf{f}}^g. \tag{28}$$

The symbol $\odot$ denotes elementwise multiplication; the node–device incidence matrices $\mathbf{\Gamma}^{GG}$ and $\mathbf{\Gamma}^{CHP}$ map each conversion device to its assigned gas node. Pipe capacity limits are adopted directly from the source case data and scaled by the same factor $E_g = 120$ MWh-eq per source unit, without a square-root transformation. This is a case-study scaling convention applied to the linear dispatch layer; the LP does not solve Weymouth equations or compressor dynamics.

The DHS6 heat interface has fixed supply-to-load pipe orientations:

$$\mathbf{A}_h\mathbf{f}_t^h + \mathbf{\Gamma}_h^{CHP}\mathbf{h}_t^{CHP} + \mathbf{\Gamma}_h^{EB}\mathbf{h}_t^{EB} - \mathbf{d}_t^h = \mathbf{0}, \tag{29}$$

$$\mathbf{0} \le \mathbf{f}_t^h \le \overline{\mathbf{f}}^h. \tag{30}$$

This representation preserves source–load connectivity and pipe capacities but omits temperature decay, transport delay, and hydraulic pressure.

At the device level, gas-fired generation satisfies

$$g_{i,t}^{GG} = \gamma_i^{GG} p_{i,t}^{GG}. \tag{31}$$

For each CHP unit i, its continuous operating region is represented by

$$p_{i,t}^{CHP} = \sum_{k \in \mathcal{K}_i} \alpha_{i,k,t} P_{i,k}^{CHP}, \tag{32}$$

$$h_{i,t}^{CHP} = \sum_{k \in \mathcal{K}_i} \alpha_{i,k,t} H_{i,k}^{CHP}, \tag{33}$$

$$\sum_{k \in \mathcal{K}_i} \alpha_{i,k,t} = 1, \qquad \alpha_{i,k,t} \ge 0. \tag{34}$$

The network model uses the four (P, H) vertices $(0, 100)$, $(100, 85)$, $(260, 320)$, and $(0, 390)$ MW and therefore assumes that the CHP unit remains online over the scheduling horizon; binary startup and shutdown decisions are outside the scope of the continuous LP. Electric-boiler conversion is

$$h_{i,t}^{EB} = \eta_i^{EB} p_{i,t}^{EB}, \qquad 0 \le h_{i,t}^{EB} \le \overline{H}_i^{EB}. \tag{35}$$

The source-consistent values are $\eta_i^{EB} = 0.85$ and $\overline{H}_i^{EB} = 50$ MW.

To use the fitted macro loss representation without extrapolation, the network actions are mapped to a bounded flexibility equivalent:

$$f_t^{\text{net}} = 65 \sum_{k \in \mathcal{K}_f} \omega_k \frac{y_{k,t} - \underline{y}_k}{\overline{y}_k - \underline{y}_k}, \qquad \boldsymbol{\omega} = (0.10, 0.10, 0.20, 0.20, 0.40), \tag{36}$$

where $\boldsymbol{y} = (p_1^{GG}, p_2^{GG}, p^{CHP}, h^{CHP}, h^{EB})$ and the normalization limits are the corresponding source-case bounds. Consequently, $0 \le f_t^{\text{net}} \le 65$ MW by construction. The same variable range is used to fit the macro loss surrogate. Generation, gas-well, reserve, demand-response, and device-capacity bounds are included in $h_t(x_t, u_t)$. Their numerical values are reported with the case-study data. Together, Equations (25)–(35) define a linear network-dispatch model rather than a nonlinear AC/gas/thermal-hydraulic simulator.

2.5. Adaptive Risk-Budget Receding-Horizon Dispatch

At operating period t, define the truncated horizon $\mathcal{H}_t = \{t, \ldots, \min(t + H - 1, N_T)\}$. The rolling problem is

$$\min_{\boldsymbol{x},\boldsymbol{\eta},\boldsymbol{s}} \sum_{\tau \in \mathcal{H}_t} C_\tau(x_\tau, u_\tau) \tag{37}$$

subject to

$$x_\tau \in \Omega_\tau^{SR}(u_\tau), \qquad \forall \tau \in \mathcal{H}_t, \tag{38}$$

$$(x_{\tau-1}, x_\tau) \in \mathcal{X}_\tau^{\text{inter}}, \qquad \forall \tau \in \mathcal{H}_t, \tag{39}$$

where $\mathcal{X}_\tau^{\text{inter}}$ contains ramping and other state-transition constraints. Only the first-period decision is implemented; the information state is then updated, and the horizon advances by one period. The implemented horizon is $H = 6$ h. The primary baseline is rolling CVaR-constrained dispatch with the same horizon, forecast updates, resource limits, and loss representation.

Let P_t^L be forecast electric demand, σ_t the normalized forecast-uncertainty signal, and s_t^g the normalized gas-stress signal. The state-dependent stress index is

$$\begin{aligned} \phi_t = a_L \min\left\{1, \frac{\pi_t}{0.85}\right\} + a_\sigma \min\left\{1, \frac{\sigma_t}{0.12}\right\} \\ + a_g \min\left\{1, \frac{s_t^g}{0.30}\right\}, \\ a_L + a_\sigma + a_g = 1, \qquad a_j \ge 0. \end{aligned} \tag{40}$$

The baseline assigns $a_L = a_\sigma = a_g = 1/3$. Equal weights are used as a neutral starting point because the three inputs are independently normalized and truncated and no empirical evidence is available to privilege one stress channel. The normalization thresholds are the upper ends of the case-study operating ranges, not estimated universal thresholds. Alternative load-, uncertainty-, and gas-dominant weights are tested in Section 4.3.

The expected-loss and CVaR cap fractions are updated separately:

$$\rho_t^E = \max\left\{\rho_{\min}, \rho_0^E(1 - \kappa\phi_t)\right\}, \tag{41}$$

$$\rho_t^C = \max\left\{\rho_{\min}, \rho_0^C(1 - \kappa\phi_t)\right\}. \tag{42}$$

For $q \in \{E, C\}$, let $R_{t,\text{low}}^q$ be the risk index evaluated at the minimum resource vector

$$(r_t, d_t, f_t) = (10, 0, 0) \text{ MW}.$$

For the macro model, $R_{t,\text{high}}^q$ is evaluated at the component-wise largest resource vector reachable within the rolling horizon after applying the resource bounds and ramp limits. For the network model, it is evaluated at the explicit ramp-bounded reference vector listed in the parameter settings of Section 3.5.

That vector is used only as a cap-normalization anchor and is not claimed to be a jointly feasible network schedule; joint feasibility is imposed by the complete network LP. The actual cap is

$$\overline{R}_t^q = R_{t,\text{high}}^q + \rho_t^q \max\left\{0, R_{t,\text{low}}^q - R_{t,\text{high}}^q\right\}, \qquad q \in \{E, C\}. \tag{43}$$

Thus, a smaller cap fraction moves the admissible risk limit toward the high-reference risk level and is more restrictive. The same loss representation, buffer, and reference construction are used in the fixed- and adaptive-budget comparisons. In the reported case, $\rho_0^E = \rho_0^C = 0.30$, $\rho_{\min} = 0.16$, and $\kappa = 0.55$. The response factor κ controls how quickly the cap tightens with stress, while $\rho_{\min}$ prevents unlimited tightening and protects feasibility when all three stress channels are high. These values are case-study design settings rather than empirically estimated constants; Section 4.3 varies κ from 0.35 to 0.75 and $\rho_{\min}$ from 0.12 to 0.20. The quantile buffer and adaptive budget play distinct roles: the former reduces held-out underprediction by the affine representation, whereas the latter tightens the admissible domain under stressed operating conditions.

At each hour, the realized forecast error of the current hour is observed and propagated over the future horizon with an exponentially decaying persistence factor. Future realized values are not supplied to the optimizer. The updated load, renewable, gas-stress, uncertainty, equivalent-residual, and availability signals define u_t. Equations (40)–(43) update the limits, after which the horizon problem (37)–(39) is solved. The first-hour decision is executed, the state and diagnostic risk measures are updated, and the procedure is repeated. The continuous LP is solved with the HiGHS solver through SciPy's linprog interface.

2.6. Risk-Limit Sensitivity and Resource-Based Mitigation Cost

For the continuous dispatch problem, let

$$J^*(\overline{R}^E, \overline{R}^C, \underline{M}) = \min_x C(x) \tag{44}$$

subject to the physical constraints, $R^E(x) \le \overline{R}^E$, $R^C(x) \le \overline{R}^C$, and $M(x) \ge \underline{M}$. Under strong duality and regularity, the dual multipliers associated with the expected-loss and CVaR constraints satisfy

$$\lambda^E = -\frac{\partial J^*}{\partial \overline{R}^E}, \qquad \lambda^C = -\frac{\partial J^*}{\partial \overline{R}^C}, \tag{45}$$

where the derivatives are understood locally and under the constraint scaling used in the LP. These quantities are reported as shadow sensitivities, not market-clearing prices.

To provide a separate local resource diagnostic, one resource coordinate $k \in \{\text{reserve}, \text{DR}, \text{cross-carrier}\}$ is increased by $\Delta = 5$ MW while the other two coordinates are held fixed. The perturbation is used only if it remains within the corresponding resource bound. For risk index $q \in \{E, C\}$, define

$$\begin{aligned} \Delta C_{t,k} &= C_t(x_t + \Delta e_k) - C_t(x_t), \\ \Delta R_{t,k}^q &= R_t^q(x_t) - R_t^q(x_t + \Delta e_k), \\ \mu_{t,k}^q &= \frac{\Delta C_{t,k}}{\Delta R_{t,k}^q}. \end{aligned} \tag{46}$$

Equation (46) is evaluated only when both the cost increment and risk reduction are positive and exceed the numerical tolerance. The lowest positive value across the three resources is reported. The dispatch problem is not re-optimized for this one-coordinate

perturbation; the resulting ratio is therefore a local resource-response diagnostic rather than a system-wide marginal value or a dual variable.

3. Case Study and Experimental Design

3.1. Experimental Framework

The numerical experiments are designed to answer two questions. First, does embedding security-margin, scenario-weighted expected-loss, and CVaR limits in the feasible domain improve risk control, and what operating-cost increase is required? Second, does the resulting scheduling logic remain feasible when the locations and transfer capacities of the electricity, gas, and heat networks are represented explicitly?

Two complementary models are used. The macro-equivalent model provides a controlled environment for comparing dispatch formulations under identical 24 h load, renewable-generation, price, contingency, and cost inputs. It is also used for the rolling-horizon comparison, ablation studies, risk-cap sensitivity analysis, forecast-error tests, and resource-response diagnostics. The network model transfers the same security–risk constraints to a coupled IEEE 39-bus–Belgian 20-node–DHS 6-node system. The resulting schedules are then checked against the complete linear bus–node–pipe topology. This two-level design separates evaluation of the proposed decision mechanism from evaluation of its consistency with the stated linear network constraints.

The nominal profiles contain 24 hourly values of electric and heat demand, renewable generation, energy price, forecast uncertainty, and gas-supply stress. In the rolling experiments, each optimization covers a 6 h horizon and implements only the first-hour decision. The horizon is then advanced by one hour, and the information state is updated. Forecast-error robustness is evaluated using 30 paired random seeds so that the compared rolling methods receive the same forecast and realization sequences.

3.2. Test Systems

The macro-equivalent LP represents reserve, demand response, and cross-carrier corrective capacity as the three controllable risk-mitigation resources. Their bounds and ramp limits are reported in the parameter settings of Section 3.5.

The security margin and contingency-loss representation follow Equations (5) and (18), respectively.

As shown in Figure 4, the network-transfer case couples a five-node electrical interface equivalent of the modified IEEE 39-bus system with the Belgian20 and DHS6 systems. Electrical interface nodes 24, 30, 33, 37, and 39 connect conventional generation, gas-fired generation, CHP production, electric-boiler consumption, and renewable injections. The Belgian20 system contains 20 nodes, 19 capacity-limited pipes, and six gas wells. Gas-fired units and the CHP unit are connected at gas nodes 6, 19, and 3, respectively. The DHS6 component connects the CHP and electric boiler to three heat-load nodes. The dispatch model enforces the linear carrier balances, interface capacities, and conversion relations in Section 2.4. The complete IEEE 39-bus topology is used only in the subsequent post-dispatch linear consistency check. Neither stage includes nonlinear AC power flow, Weymouth gas hydraulics, compressor dynamics, or transient district-heating processes.

3.3. Contingency Selection and Scenario Weights

Four contingencies are retained by consequence screening. Let S_z denote the raw screening consequence for contingency z. Its relative severity and normalized scenario weight are calculated as

$$\widetilde{S}_z = \frac{S_z}{\max_{j \in \mathcal{Z}} S_j}, \qquad w_z = \frac{S_z}{\sum_{j \in \mathcal{Z}} S_j}. \tag{47}$$

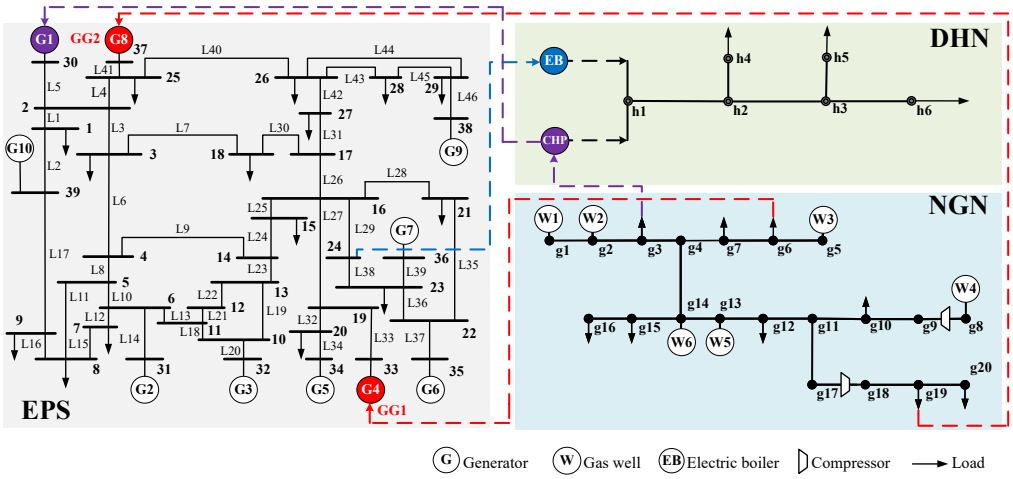

Figure 4. Detailed topology and coupling interfaces of the modified IEEE 39-bus, Belgian20, and DHS6 test system. The rolling-dispatch model uses the five-node electrical interface equivalent associated with buses 24, 30, 33, 37, and 39; the complete IEEE 39-bus topology is retained only for the post-dispatch linear consistency check.

The weights preserve the consequence ranking of the screening stage but are not empirical outage probabilities. Because both S_z and the loss labels encode consequence, this weighting deliberately emphasizes severe screened events and may count severity in both the weight and the loss magnitude. Accordingly, the resulting expected-loss and CVaR values are interpreted only as comparative scenario-weighted dispatch-risk indices. Uniform and severity-tempered alternatives are evaluated in the sensitivity analysis. Table 3 lists the retained contingencies and their weights.

Table 3. Screened contingencies and normalized consequence weights.

Scenario	Screened Event	Primary Affected Carriers	Risk Role	$\widetilde{S}_z$	w_z
C1	W4 gas-source outage	Gas, electricity, and heat	Dominant gas-supply event	1.000	0.6755
C2	W6 gas-source outage	Gas, electricity, and heat	Secondary gas-supply event	0.448	0.3025
C3	Electric-interface outage	Electricity and coupled heat supply	Low-weight electric event	0.016	0.0110
C4	Cross-energy-interface disturbance	Gas, heat, and coupled electricity supply	Low-weight coupling event	0.016	0.0110

Because the four-scenario set is strongly concentrated in C1 and C2, the main case is supplemented by a tail-stress experiment. Each parent contingency is expanded into constructed normal, severe, and extreme conditional branches, and the CVaR confidence level is raised from 0.75 to 0.85, so that the two risk metrics are compared when losses concentrate in a smaller tail. Every variant uses the same 6 h rolling LP, ramp limits, security-margin constraint, affine loss epigraph, and conservative buffer; the expected-loss and CVaR constraints are removed one at a time, and no risk penalty is added to the objective. The conditional branch weights are synthetic: they serve to separate the two risk metrics in a controlled comparison and imply no annual reliability interpretation.

3.4. Compared Dispatch Formulations

Five formulations are compared by progressively adding the constraints defined in Section 2.2. Economic dispatch (ED) contains only the physical dispatch constraints. Security-constrained economic dispatch (SCED) adds the security-margin floor. Expected-risk dispatch (ERD) further adds the scenario-weighted expected-loss limit. CVaR-

constrained risk dispatch (CVaR-RD) adds the CVaR limit with fixed cap fractions. The proposed method uses the same buffered loss representation and security–risk constraints but updates the expected-loss and CVaR cap fractions according to the operating stress index.

Table 4 reports the actual configuration of each method. The static 24 h cases illustrate how the nested constraint sets alter the admissible dispatch domain. The primary effectiveness test compares rolling CVaR-RD with the proposed rolling method. Both use the same 6 h horizon, forecast-update rule, robust forecast adjustment, resource bounds, ramp limits, scenario weights, and buffered loss representation; the adaptive risk budget is the only structural difference.

Table 4. Configuration of the compared dispatch formulations.

Method	Margin Floor	Expected Cap	CVaR Cap	Adaptive Caps	Purpose
ED	–	–	–	No	Economic reference
SCED	0.18	–	–	No	Effect of deterministic security
ERD	0.18	0.30	–	No	Effect of average-consequence control
CVaR-RD	0.20	0.30	0.30	No	Fixed average- and tail-risk limits
Proposed	0.20	0.30	0.30	Yes	State-adaptive security–risk dispatch

3.5. Parameter Settings and Evaluation Metrics

Table 5 summarizes the parameter values used in the reported experiments. The main CVaR confidence level is $\alpha = 0.75$, which corresponds to a tail mass of 0.25 in the four-scenario weighted distribution. The nominal expected-loss and CVaR cap fractions are both 0.30. For the proposed method, the adaptive strength is $\kappa = 0.55$, and the cap fraction is bounded below by $\rho_{\min} = 0.16$. As defined in Equation (43), these fractions interpolate between the risk levels associated with the minimum resource vector and the high-reference vector. Lower fractions therefore impose tighter limits.

The principal performance indicators are total operating cost, cumulative scenario-weighted expected loss, maximum hourly CVaR, minimum hourly security margin, and average deployment of reserve, demand response, and cross-carrier flexibility. LP dual multipliers are reported as local risk-limit sensitivities. The 5 MW one-coordinate finite differences are reported separately as local resource-response diagnostics. Solution time is used to assess computational tractability. Carbon output is included as a secondary indicator. A transparent internal carbon-cost coefficient enters the objective, but neither a carbon cap nor a separate carbon-minimization objective is imposed.

Table 5. Parameters used in the reported dispatch experiments.

Parameter	Value	Use in the Experiments
Scheduling period	24 h, 1 h resolution	Static and rolling evaluations
Rolling horizon H	6 h	First-hour implementation and hourly update
Main CVaR level α	0.75	Four-scenario dispatch-risk calculation
Tail-stress CVaR level	0.85	Expanded-branch tail-stress test
Nominal cap fractions (ρ_0^E, ρ_0^C)	$(0.30, 0.30)$	Fixed caps and starting values of adaptive caps
Minimum cap fraction $\rho_{\min}$	0.16	Lower bound on adaptive tightening
Adaptive strength κ	0.55	Stress-dependent adjustment of cap fractions
Reserve bound	10–95 MW	Corrective reserve capacity
Demand-response bound	0–30 MW	Controllable load adjustment

Table 5. *Cont.*

Parameter	Value	Use in the Experiments
Cross-carrier flexibility bound	0–65 MW	Macro-equivalent coupling response
Network gas scaling E_g	120 MWh-eq/source unit	Source-unit and pipe-limit mapping in the dispatch layer
Electric boiler	$\eta^{EB} = 0.85$, $\overline{H}^{EB} = 50$ MW	Source-consistent electricity-to-heat conversion
Network risk-reference vector	Reserve 95 MW; DR 30 MW; GG1 300 MW; GG2 260 MW; CHP power 220 MW; CHP heat 320 MW; EB input 58.82 MW	Upper references used only for adaptive-cap interpolation
Resource ramp limits	25/15/25 MW h^{-1}	Reserve/DR/cross-carrier intertemporal limits
Loss buffer	Contingency-specific 95th percentile	Held-out positive underprediction, scaled by operating state
Forecast-error comparison	30 paired seeds	Common realizations for both rolling methods
Solver	HiGHS (via SciPy's linprog interface)	Continuous linear-programming solution

4. Results and Discussion

4.1. Adaptive Rolling-Dispatch Performance

The primary evaluation uses the paired comparison defined in Section 3.4; Table 6 reports the mean and standard deviation across 30 forecast-error realizations.

Table 6. Fair rolling comparison under common 6 h horizons and information updates (mean ± standard deviation across 30 paired seeds).

Method	Cost (10^4 CNY)	WUEI (MWh)	Max CVaR (MWh)	Min Margin	Reserve (MW)	DR (MW)	Cross-Carrier (MW)
Rolling CVaR-RD	753.38 ± 9.28	143.06 ± 3.27	10.68 ± 0.77	0.229 ± 0.013	25.37 ± 0.37	25.02 ± 0.09	39.98 ± 0.07
Rolling equal-mean-budget CVaR-RD	770.28 ± 9.53	136.15 ± 3.02	10.31 ± 0.76	0.247 ± 0.014	33.61 ± 0.17	25.00 ± 0.00	49.59 ± 0.21
Rolling proposed	769.51 ± 9.49	136.08 ± 2.99	10.21 ± 0.76	0.251 ± 0.014	32.60 ± 0.27	25.00 ± 0.00	49.49 ± 0.18

Relative to rolling CVaR-RD, the adaptive-budget method reduces cumulative WUEI and maximum hourly CVaR by 4.88% and 4.38%, respectively, while increasing operating cost by 2.14%. The minimum security margin increases from 0.229 to 0.251. WUEI and CVaR improve in 30/30 and 30/30 paired realizations, respectively. The seed-level WUEI reductions range from 4.46% to 5.16%, and the CVaR reductions range from 1.75% to 8.34%. The paired CVaR difference is −0.467 MWh (95% CI: −0.526 to −0.409 MWh).

The fixed 0.30 benchmark combines the effects of temporal allocation and overall cap tightening. To isolate the former, the equal-mean-budget benchmark uses a constant cap fraction equal to the 24 h mean of the adaptive fractions for each paired realization. Relative to this benchmark, the proposed method reduces WUEI and maximum hourly CVaR by 0.05% and 0.91%, respectively, with a −0.10% cost change. The paired differences (proposed minus equal-budget) are −0.070 MWh for WUEI (95% CI: −0.101 to −0.039 MWh) and −0.094 MWh for CVaR (95% CI: −0.108 to −0.079 MWh). The CVaR improvement occurs in 30/30 pairs. These results support a statistically detectable but operationally modest benefit from temporal budget allocation. In absolute mean terms, moving from the fixed 0.30 cap to the proposed method reduces WUEI from 143.06 to 136.08 MWh and maximum hourly CVaR from 10.68 to 10.21 MWh, reductions of 6.98 and 0.47 MWh. Moving from the equal-mean cap to the proposed temporal allocation reduces the same indices from 136.15 to 136.08 MWh and from 10.31 to 10.21 MWh, respectively. Thus, temporal allocation

accounts for approximately 1% of the total WUEI improvement and 21% of the total maximum-CVaR improvement relative to the fixed 0.30 cap. It also lowers mean operating cost by 0.77 $\times$ 10^4 CNY relative to the equal-mean benchmark. The practical interpretation is therefore not a large energy-savings effect; it is a small redistribution of corrective effort toward the hours that determine the daily tail-risk metric.

The risk reduction is achieved mainly through additional reserve and cross-carrier flexibility. Average reserve increases by 7.23 MW, whereas cross-carrier corrective capacity increases by 9.51 MW. Demand response is already close to its upper bound under rolling CVaR-RD and consequently changes little. Figure 5 confirms that the adaptive budget primarily affects stressed hours: it increases corrective resources, raises the security margin, and suppresses the upper CVaR trajectory. This pattern is consistent with the mechanism of Equation (43): tighter state-dependent caps move the solution toward the high-reference risk level.



Figure 5. Paired rolling comparison across 30 common forecast-error seeds. Lines show hourly means and shaded bands show one standard deviation. Both methods use the same 6 h horizon and information updates; only the proposed method adapts the risk caps.

To isolate constraint layering from the rolling implementation, the five formulations are also solved using a common 24 h static information structure. The results are reported in Table 7. In this controlled comparison, the proposed adaptive-cap formulation increases cost from 682.37 to 787.30 in $\times 10^4$ CNY, reduces cumulative WUEI from 174.93 to 125.51 MWh, reduces maximum hourly CVaR from 12.47 to 8.62 MWh, and raises the minimum security margin from 0.096 to 0.279. These changes correspond to a 15.38% cost increase and reductions of 28.25% and 30.82% in WUEI and CVaR, respectively.

ERD and fixed-cap CVaR-RD select the same operating point in the nominal four-scenario case. This equality reflects active-set redundancy under the highly concentrated scenario weights; it does not imply that expected loss and CVaR are generally interchangeable. Their distinct roles are examined below using the tail-stress experiment of Section 3.3.

Table 7. Constraint -layering comparison under a common 24 h static information structure.

Method	Cost (10^4 CNY)	WUEI (MWh)	Max CVaR (MWh)	Min Margin	Reserve (MW)	DR (MW)	Flex (MW)
ED	682.37	174.93	12.47	0.096	10.00	0.00	0.00
SCED	694.33	165.89	11.24	0.180	14.91	18.60	0.00
ERD	773.60	131.06	9.05	0.273	33.63	25.00	52.82
CVaR-RD	773.69	131.02	9.05	0.273	31.55	25.00	54.06
Proposed	787.30	125.51	8.62	0.279	47.35	25.00	56.58

4.2. Risk-Constraint Activity and Tail-Risk Control

The expected-loss and CVaR constraints exhibit markedly different activation patterns. In the nominal rolling case, the expected-loss constraint has a positive dual multiplier in 16 h, whereas the CVaR constraint has a positive multiplier in 8 h. The median positive CVaR dual is 18.34 model-cost units per MWh-risk. The isolated expected-loss dual at hour 8 is highly sensitive to constraint scaling and local degeneracy; it is therefore reported only as a numerical sensitivity diagnostic. Activation counts and medians are more informative than an arithmetic mean for these sparse, heavy-tailed dual values.

The 5 MW finite differences provide a separate local resource-response diagnostic. One resource coordinate is increased by 5 MW while the remaining coordinates are held fixed, without re-optimizing the complete dispatch problem. The median positive cost-to-risk ratios are 23.51 and 17.64 CNY per MWh-risk for the expected-loss and CVaR indices, respectively. These quantities describe the local response of the fitted cost and risk functions. Figure 6 therefore reports the finite differences as local response ratios and displays them on a logarithmic scale.

One-at-a-time removal of the security-margin, expected-loss, or CVaR constraint leaves the nominal solution unchanged to the reported precision because the remaining constraints support the same active boundary. The meaningful ablations are the joint removal of both risk limits and replacement of the adaptive budget by fixed caps. As shown in Table 8, removing both risk limits changes cost by −8.05% and changes WUEI, CVaR, and the minimum margin by 20.68%, 14.74%, and −23.80%, respectively. Replacing adaptive caps with fixed caps changes the same four quantities by −2.01%, 4.92%, 3.57%, and −8.20%.

Table 8. Mechanism -revealing ablations relative to the proposed rolling method.

Variant	Cost Change (%)	WUEI Change (%)	CVaR Change (%)	Margin Change (%)
No expected-loss or CVaR limits	−8.05	20.68	14.74	−23.80
Fixed risk caps	−2.01	4.92	3.57	−8.20

Removing the quantile buffer rescales the reported risk indices and is therefore not interpreted as an operational improvement. Instead, the distinct function of CVaR is identified under a common hard-constraint rolling formulation by expanding each parent contingency into constructed normal, severe, and extreme branches. In this tail-stress experiment, removing the CVaR constraint increases WUEI by 17.48% and maximum hourly CVaR by 79.63% relative to the complete formulation. The tail-risk-only variant keeps maximum hourly CVaR at 7.61 MWh, equal to the rounded complete value of 7.61 MWh, whereas the expected-risk-only variant reaches 13.68 MWh.

These results clarify the complementary roles of the two risk limits, as separated in Figure 7. The weighted unserved-energy limit controls distributed consequence across the screened branches, whereas CVaR becomes discriminating when losses are concentrated in a small number of severe branches. CVaR is therefore useful beyond WUEI only when the scenario representation contains meaningful tail heterogeneity.

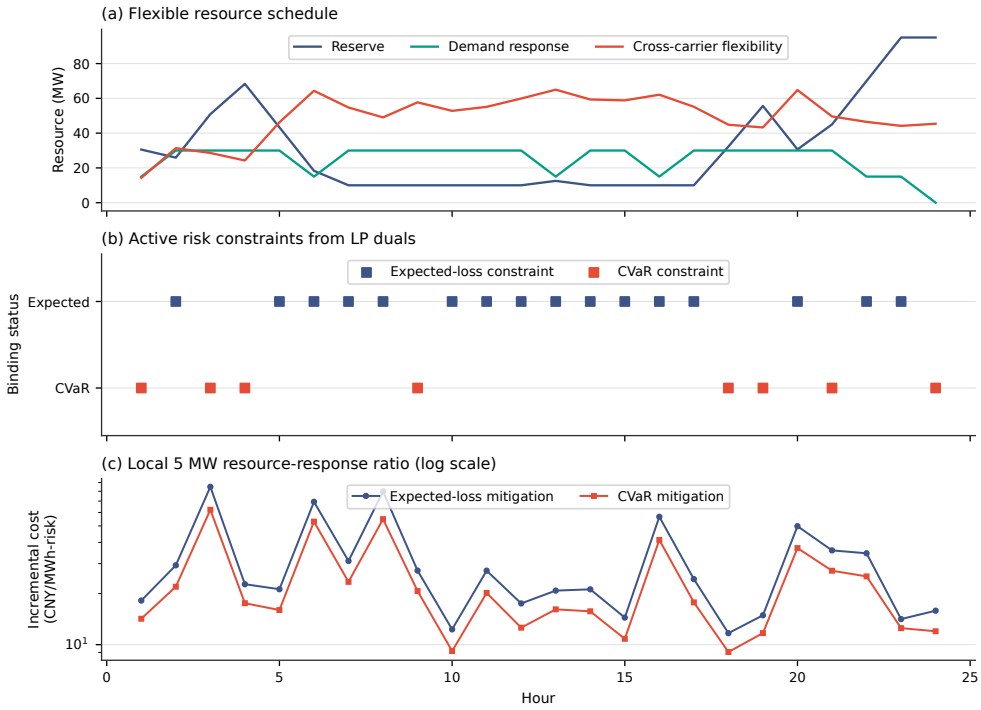

Figure 6. Flexible-resource response and risk-constraint diagnostics. Panel (**a**) shows scheduled corrective resources, panel (**b**) identifies hours with positive risk-constraint duals, and panel (**c**) reports one-coordinate 5 MW local resource-response ratios.

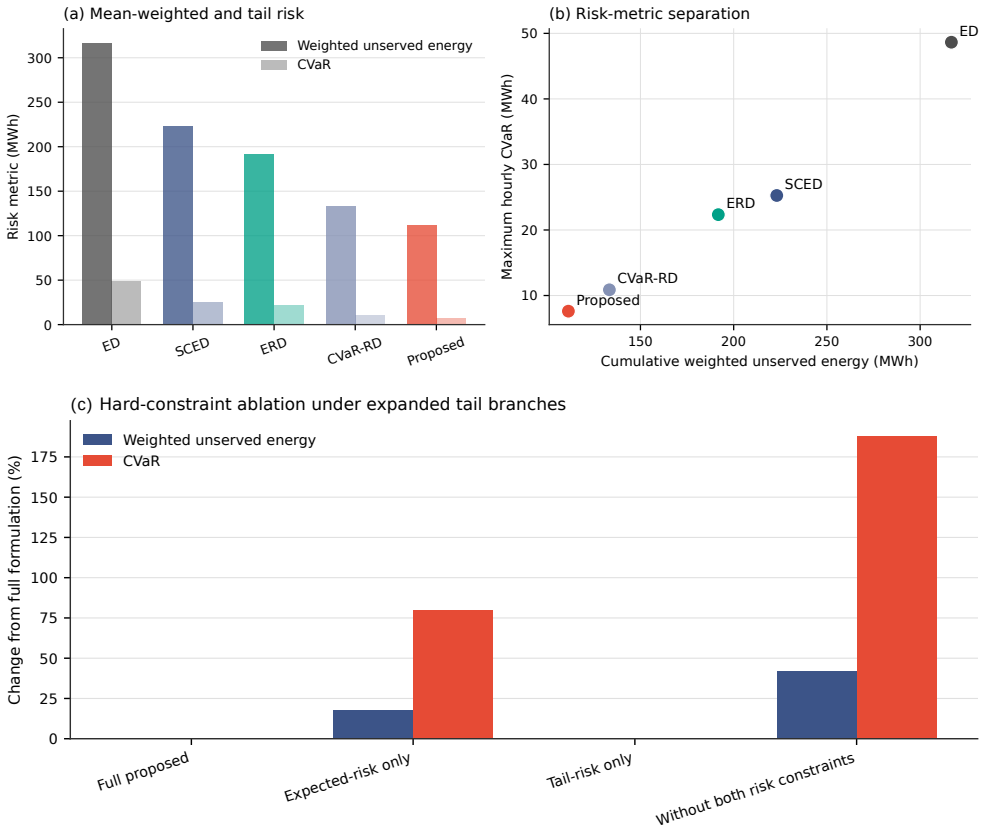

Figure 7. Separation of expected loss and CVaR under the tail-stress experiment. The conditional branches are constructed for mechanism identification and are not observed accident frequencies.

4.3. Sensitivity and Robustness

The cap-fraction sweep produces the expected cost–risk frontier. Figure 8 plots this frontier. Tightening the common cap fraction from 0.70 to 0.26 increases cost from 708.90 to 759.85 $\times$ 10^4 CNY, reduces WUEI from 159.28 to 136.82 MWh, reduces maximum hourly CVaR from 10.84 to 9.67 MWh, and raises the minimum margin from 0.209 to 0.255. This direction is consistent with the nested-domain property: lower cap fractions move the risk bounds toward the high-resource risk level, shrink the admissible domain, and cannot reduce the minimum operating cost.

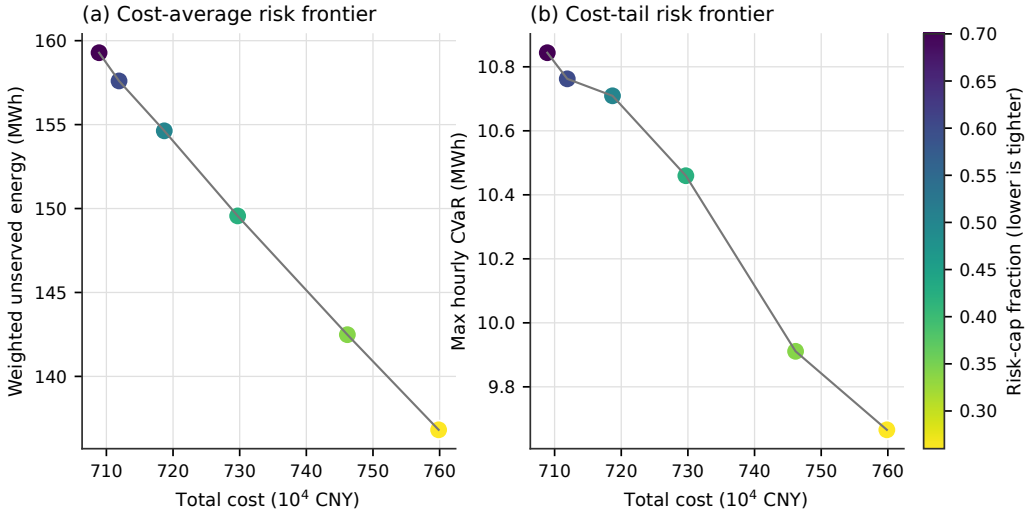

Figure 8. Cost–risk frontier under cap-fraction tightening. Lower fractions represent tighter expected-loss and CVaR limits.

The same qualitative improvement is obtained under forecast-error, peak-load, and renewable-rich conditions. Across the 30 forecast-error seeds, the proposed method yields WUEI between 129.62 and 140.83 MWh and maximum hourly CVaR between 8.67 and 11.85 MWh. Under the peak-load condition, WUEI and CVaR decrease from 213.39 MWh and 15.08 MWh under ED to 160.83 MWh and 11.33 MWh under the proposed method. Under the renewable-rich condition, they decrease from 174.75 MWh and 12.32 MWh to 132.75 MWh and 9.33 MWh. These results demonstrate directional robustness across the tested forecast, peak-load, and renewable conditions; the conclusions are drawn only within those tested ranges.

The probability/weight sensitivity uses 5 reproducible sets: consequence-normalized, uniform, failure-rate proxy, hybrid proxy, and severity-tempered proxy weights. Relative to ED under the same set, the proposed formulation reduces WUEI by 23.03–23.88% and the maximum hourly CVaR index by 23.95–24.19%. The consequence-weight cap-normalization reference is held fixed while evaluation weights vary, so the test does not renormalize the risk limits for each weight set. These proxy cases show moderate rather than invariant sensitivity and do not constitute empirical outage-probability validation.

Table 9 broadens the test to the stress index, adaptive-map settings, security-index coefficients, and contingency composition. Percentages are paired changes of the proposed method relative to the fixed-cap rolling method under the same setting; a negative WUEI or CVaR change is favorable.

All 33 paired settings are feasible, and the proposed method retains lower WUEI, lower maximum CVaR, and a higher minimum security margin than the corresponding fixed-cap case. Among the leave-one-out tests, removing C1 changes the absolute risk indices most because C1 has the largest consequence scale, but it does not reverse the

method ranking. These tests support directional robustness within the stated ranges, not global parameter invariance.

Table 9. Parameter and modeling-assumption sensitivity relative to the paired fixed-cap rolling method.

Test Family	Settings	Cost Change (%)	WUEI Change (%)	Max-CVaR Change (%)
Stress weights	Equal; load-, uncertainty-, gas-dominant	+1.74–+2.28	−5.11–−4.20	−4.11–−2.99
Response factor κ	0.35, 0.45, 0.55, 0.65, 0.75	+1.31–+2.68	−6.03–−3.03	−4.34–−2.21
Floor $\rho_{\min}$	0.12, 0.14, 0.16, 0.18, 0.20	+1.93–+2.05	−4.69–−4.42	−3.45–−3.13
Security coefficients	Each coefficient at ±20%	+2.00–+2.05	−4.69–−4.60	−3.67–−3.45
Contingency composition	All scenarios and four leave-one-out cases	+1.96–+3.43	−5.72–−4.69	−7.92–−3.37

4.4. Network Transfer and Post-Dispatch Topology Check

The IEEE 39-bus–Belgian 20-node–DHS 6-node experiment transfers the fitted-and-buffered risk representation to the interface-equivalent dispatch model with explicit gas and heat nodes, conversion-device locations, and capacity-limited electrical interfaces. As in the macro case, constraint layering and adaptive-budget performance are evaluated separately. Table 10 uses a common 24 h static information structure, whereas Table 11 compares fixed and adaptive risk caps under identical 6 h rolling settings.

Table 10. Descriptive results of the linear network-transfer experiment.

Method	Cost	WUEI	CVaR	Margin	Reserve	DR	GG Power	CHP Heat	EB Heat
ED	132.85	162.60	11.23	0.281	10.00	0.00	471.97	338.99	0.21
SCED	132.85	162.64	11.25	0.281	10.00	0.00	471.97	338.99	0.21
ERD	215.74	133.27	9.25	0.403	87.59	14.17	441.23	329.30	9.89
CVaR-RD	216.30	133.15	9.25	0.403	86.54	14.32	440.64	328.42	10.78
Proposed	233.70	128.57	8.91	0.409	89.00	17.88	430.92	319.38	19.82

Under the common static setting, the expected-loss constraint activates reserve, demand response, gas-fired redispatch, and electric-boiler heat. ERD and fixed-cap CVaR-RD produce similar but independently constrained solutions in this four-scenario case. Relative to ED, the static adaptive-cap formulation reduces WUEI from 162.60 to 128.57 MWh-eq and maximum hourly CVaR from 11.23 to 8.91 MWh-eq while raising the minimum security margin from 0.281 to 0.409.

Table 11. Fair network rolling comparison under common 6 h horizons and information updates.

Method	Cost	WUEI	CVaR	Margin	Reserve	DR	CHP Heat	EB Heat
Rolling CVaR-RD	195.88	139.86	9.66	0.389	78.03	7.89	335.34	3.85
Rolling equal-mean-budget CVaR-RD	216.59	133.43	9.31	0.418	84.87	13.51	328.04	11.15
Rolling proposed	218.83	132.76	9.14	0.412	86.00	13.20	326.68	12.51

Under this controlled rolling comparison, adaptive caps reduce WUEI by 5.08% and maximum hourly CVaR by 5.48%, while the minimum security margin increases by 5.79%. The associated operating-cost increase is 11.71%. The larger cost premium than in the macro model reflects the explicit nodal balances, pipe capacities, device locations, and restricted substitution among networked resources. Average reserve increases from 78.03 to 86.00M̃W, demand response from 7.89 to 13.20M̃W, and electric-boiler heat from 3.85 to 12.51 MW. Figure 9 shows the cross-carrier actions deployed in the linear network experiment. The normalized network flexibility equivalent remains between 23.06 and 52.28 MW,

which is inside the 0–65 MW surrogate calibration domain. The gas pipes are not binding in this case; the maximum linear gas-pipe loading is 0.460 p.u. The example therefore demonstrates network-consistent resource allocation but without exhibiting gas congestion.

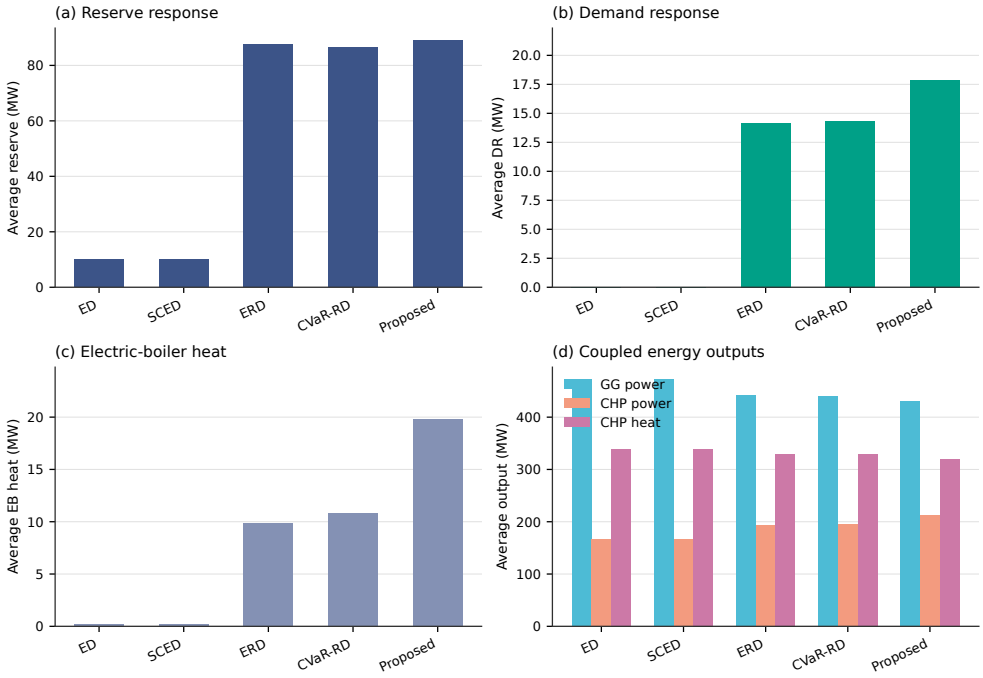

Figure 9. Cross-carrier actions in the linear network experiment. Reserve and gas-fired generation provide most of the risk-reduction response, while electric-boiler heat represents the electricity-to-heat interface.

The source-data audit is summarized in Table 12. The gas-branch dataset reports a pipe-capacity value of 5.0000 source units for pipe 8, which equals 600.00 MWh-eq/h after multiplication by $E_g = 120$. The W4 upper bound is only 2.3018 source units (276.22 MWh-eq/h). Consequently, the source and pipe limits provide 323.78 MWh-eq/h of nameplate headroom and do not imply a W4 deliverability violation.

Table 12. Source-semantic check for W4 and pipe 8 in the linear Belgian20 topology.

Quantity	Source Units	MWh-eq/h	Interpretation
W4 upper bound	2.3018	276.22	Gas-source nameplate bound
Pipe-8 capacity field	5.0000	600.00	Direct source-field conversion
Pipe headroom over W4	2.6982	323.78	No source–pipe mismatch

The location-aware gas balances and all pipe limits remain in the dispatch model, but no congestion claim is made for this particular operating profile.

The post-dispatch full-topology linear check uses the independently generated hourly electricity, base-gas, and heat demands exported by the dispatch experiment, allocates them to the full node sets by the source-case shares, and reports zero additional electricity, gas, and heat shedding for all five static schedules over the complete 24 h horizon. The relaxed squared-pressure compatibility check is satisfied in 24 of the 24 h for each method. Maximum gas-pipe loading remains 0.460, while the maximum electric-line loading ranges from 0.694 to 0.739 p.u. and the maximum heat-pipe loading is 0.985 p.u. Because nodal injections are allocated by fixed reconstruction rules, this check establishes routing and linear consistency only; nonlinear AC, gas-hydraulic, and thermal-dynamic validation remain outside its scope.

The same full-topology check was then applied to the three rolling schedules in Table 11, rather than only to the five static schedules. Table 13 reports the complete 24 h result. No additional carrier shedding is required at nominal capacities, and the relaxed pressure-compatibility test passes in every hour.

Table 13. Full-topology linear check of the three 24 h rolling schedules at nominal network capacities.

Rolling Method	Hours	Electric Shed	Gas Shed	Heat Shed	Max Electric Load	Max Gas Load	Max Heat Load	Pressure-Compatible Hours
Fixed CVaR-RD	24	0	0	0	0.738	0.460	0.985	24/24
Equal-mean-budget CVaR-RD	24	0	0	0	0.701	0.460	0.985	24/24
Proposed	24	0	0	0	0.697	0.460	0.985	24/24

A common capacity multiplier tests sensitivity to network parameter assumptions. At multipliers 1.00 and 1.10, all three rolling schedules retain zero additional shedding. At 0.90, each schedule requires 110.00 MWh-eq of additional shedding over the day, with the heat network reaching unit loading. The shared shortfall is informative: adaptive allocation can redistribute preventive resources under available flexibility, but it cannot remove a physical heat-transfer bottleneck created by a system-wide 10% capacity derating. This limitation prevents interpreting risk-budget adaptation as a substitute for network reinforcement.

4.5. Verification, Robustness, and Validation Scope

Four evidence levels are distinguished. First, implementation verification uses fixed seeds, automated regression checks, solver feasibility, and reproduction of the submitted baseline results before introducing the new sensitivity cases. Second, the per-contingency held-out comparison in Table 2 verifies the affine emulator against its deterministic reference evaluator. Third, the static and rolling topology checks verify that reconstructed schedules satisfy the linear routing, capacity, and relaxed pressure-compatibility conditions of the source cases. Fourth, parameter, scenario-weight, contingency-composition, forecast, and capacity sweeps assess robustness within explicitly stated ranges.

These steps are verification and internal case-study consistency checks. They do not constitute external validation against historical outage observations, an independently developed nonlinear contingency simulator, or field operations. Accordingly, the numerical reductions are evidence for the tested linear framework, not estimates of real-system reliability improvement.

4.6. Computational Performance, Applicability, and Limitations

Across the rolling experiment with 30 paired seeds, the proposed macro LP requires 0.0032 s on average and 0.0085 s at most per solve on the test platform. The fair rolling network LP requires 0.0133 s on average and 0.0251 s at most, while the post-dispatch full-topology linear check requires approximately 0.0042 s per hourly evaluation. The tail-stress experiment uses the same rolling LP architecture with ten conditional branches; the proposed case requires approximately 0.0045 s on average and 0.0068 s at most. These runtimes establish tractability for the tested continuous linear models; scalability to mixed-integer commitment or nonlinear network physics is not addressed.

Operationally, the embedded expected-loss and CVaR limits translate screened contingency consequences into preventive resource deployment and identify how reserve, demand response, locational gas redispatch, CHP production, and electric-boiler conversion share the risk-control burden. CVaR and rolling optimization are established tools [27,28,38,40]; the contribution here is their integration into a nested admissible-domain construction with state-dependent risk caps and an explicit cross-carrier network check.

Carbon emissions are not separately capped but enter the objective through internal carbon-cost coefficients of 0.030 and 0.035 $\times 10^4$ CNY/tCO_2 for the macro and network cases, corresponding to 300 and 350 CNY/tCO_2. The reported carbon reductions, from 10,859.62 to 10,457.22 t in the macro case and from 10,500.19 to 9859.24 t in the network case, are co-optimized outcomes under assumed price scenarios rather than evidence of carbon-optimal dispatch or calibrated policy forecasts. In the macro sensitivity test, varying the internal carbon price from 0 to 900 CNY/tCO_2 changes proposed-method emissions from 10,457.31 to 10,427.18 t and cost from 736.86 to 830.69 $\times 10^4$ CNY.

The interpretation of the reported results is limited by five modeling choices. First, the network layer uses linear electric, gas-deliverability, and heat-interface constraints. Omitting reactive-power and voltage behavior can overstate electrical transfer capability; omitting Weymouth relations and compressor operation can misrepresent pressure-sensitive gas deliverability; and omitting heat-transport delay and temperature dynamics can make thermal substitution appear more immediate than it is. The topology check therefore confirms reconstructed-schedule compatibility only under the adopted linear physics. Second, the 24 h load, renewable, uncertainty, cost, and carbon inputs are synthetic case-study profiles. Their limited temporal and seasonal range means that both the size and timing of the reported cost–risk tradeoff may change on historical multi-season data. Third, the scenario weights derive from consequence screening rather than documented outage frequencies; as defined in Section 2.1, the risk indices rank dispatches within the screened catalog but cannot be interpreted as annual expected unserved energy or conventional reliability statistics. Fourth, the affine loss representation is fitted to a deterministic case-study evaluator. Its held-out errors measure emulator fidelity and may understate model-form error relative to an independent nonlinear contingency simulator or field observations. Fifth, the continuous model excludes binary commitment and discrete corrective switching. This can make flexibility deployment smoother, faster, and less costly than a unit-commitment implementation with minimum up/down times and switching restrictions.

Future work should combine empirical outage data, independently generated nonlinear loss labels, mixed-integer decisions, and nonlinear gas and thermal feasibility.

5. Conclusions

This study embeds security-margin, weighted unserved-energy, and CVaR limits in a 6 h rolling dispatch model with state-dependent risk budgets. Across 30 paired forecast-error realizations, the proposed method reduces WUEI by 4.88% and maximum hourly CVaR by 4.38% relative to fixed-cap rolling dispatch, at a 2.14% operating-cost increase. The equal-mean comparison shows where that improvement originates: temporal allocation contributes only 0.07 MWh of the 6.98 MWh total WUEI reduction but 0.10 MWh of the 0.47 MWh total maximum-CVaR reduction. Its practical value in this case is therefore a modest, systematic reallocation toward tail-determining hours rather than a large reduction in total expected loss.

The IEEE 39-bus–Belgian 20-node–DHS 6-node transfer case maintains the network flexibility equivalent within its calibrated 0–65 MW domain. All three rolling schedules pass the 24 h full-topology linear routing and relaxed pressure-compatibility checks without additional shedding at nominal capacities. However, a common 10% capacity derating produces the same 110.00 MWh-eq heat-side shortfall for all three methods, showing that adaptive risk budgets do not replace physical network adequacy. The framework is thus a tractable linear proof of concept for comparative service-continuity management. Empirical outage data, mixed-integer operating decisions, and independent nonlinear electricity–gas–heat validation are required before real-system reliability claims can be made.

From a sustainability perspective, the proposed framework addresses the environmental, economic, and social dimensions of integrated-energy operation in a balanced manner. It reduces weighted unserved energy and tail risk under stressed conditions, thereby supporting the continuity and resilience of electricity, gas, and heating services for society; it achieves these gains through a state-dependent risk budget at a modest operating-cost premium rather than unconditional over-conservatism; and it co-tracks carbon output while facilitating the efficient use of renewable and multi-carrier resources. These features provide a tractable operational mechanism through which risk-aware dispatch supports sustainable, low-carbon, and resilient energy supply.

Author Contributions: Conceptualization, J.K. and T.Q.; methodology, J.K.; software, J.K.; investigation, J.K. and T.Q.; resources, W.T. and T.Q.; data curation, J.K.; writing—original draft preparation, J.K.; writing—review and editing, W.T. and T.Q.; supervision, W.T.; project administration, W.T. All authors have read and agreed to the published version of the manuscript.

Funding: This research received no external funding.

Institutional Review Board Statement: Not applicable.

Informed Consent Statement: Not applicable.

Data Availability Statement: The reproducibility package contains the Python 3.12 programs, source case, generated CSV results, figures, and LaTeX manuscript used in this study, together with the fixed random seed used for surrogate sampling and the scenario identifiers of the consequence-screening catalog. Further inquiries can be directed to the corresponding author.

Conflicts of Interest: The authors declare no conflicts of interest.

Abbreviations

The following abbreviations are used in this manuscript:

CVaR	Conditional value-at-risk
DR	Demand response
EB	Electric boiler
ED	Economic dispatch
ERD	Expected-risk dispatch
GG	Gas-fired generator
IES	Integrated energy system
LP	Linear program
SCED	Security-constrained economic dispatch
WUEI	Weighted unserved-energy index

References

1. United Nations. Transforming Our World: The 2030 Agenda for Sustainable Development. Resolution A/RES/70/1, Adopted 25 September 2015. Available online: https://sdgs.un.org/2030agenda (accessed on 27 August 2026).
2. Geidl, M.; Andersson, G. Optimal Power Flow of Multiple Energy Carriers. *IEEE Trans. Power Syst.* **2007**, *22*, 145–155. [CrossRef]
3. Geidl, M.; Koeppel, G.; Favre-Perrod, P.; Klockl, B.; Andersson, G.; Frohlich, K. Energy Hubs for the Future. *IEEE Power Energy Mag.* **2007**, *5*, 24–30. [CrossRef]
4. Pan, Z.; Guo, Q.; Sun, H. Interactions of District Electricity and Heating Systems Considering Time-Scale Characteristics Based on Quasi-Steady Multi-Energy Flow. *Appl. Energy* **2016**, *167*, 230–243. [CrossRef]
5. Li, G.; Zhang, R.; Jiang, T.; Chen, H.; Bai, L.; Cui, H.; Li, X. Optimal Dispatch Strategy for Integrated Energy Systems with CCHP and Wind Power. *Appl. Energy* **2017**, *192*, 408–419. [CrossRef]
6. Chaudry, M.; Jenkins, N.; Strbac, G. Multi-Time Period Combined Gas and Electricity Network Optimisation. *Electr. Power Syst. Res.* **2008**, *78*, 1265–1279. [CrossRef]
7. Clegg, S.; Mancarella, P. Integrated Modeling and Assessment of the Operational Impact of Power-to-Gas (P2G) on Electrical and Gas Transmission Networks. *IEEE Trans. Sustain. Energy* **2015**, *6*, 1234–1244. [CrossRef]

8. Clegg, S.; Mancarella, P. Integrated Electrical and Gas Network Flexibility Assessment in Low-Carbon Multi-Energy Systems. *IEEE Trans. Sustain. Energy* **2016**, *7*, 718–731. [CrossRef]
9. Shabanpour-Haghighi, A.; Seifi, A.R. An Integrated Steady-State Operation Assessment of Electrical, Natural Gas, and District Heating Networks. *IEEE Trans. Power Syst.* **2016**, *31*, 3636–3647. [CrossRef]
10. Raheli, E.; Wu, Q.; Zhang, M.; Wen, C. Optimal Coordinated Operation of Integrated Natural Gas and Electric Power Systems: A Review of Modeling and Solution Methods. *Renew. Sustain. Energy Rev.* **2021**, *145*, 111134. [CrossRef]
11. Rinaldi, S.M.; Peerenboom, J.P.; Kelly, T.K. Identifying, Understanding, and Analyzing Critical Infrastructure Interdependencies. *IEEE Control Syst. Mag.* **2001**, *21*, 11–25. [CrossRef]
12. Ouyang, M. Review on Modeling and Simulation of Interdependent Critical Infrastructure Systems. *Reliab. Eng. Syst. Saf.* **2014**, *121*, 43–60. [CrossRef]
13. Zhong, J.; Tan, Y.; Li, Y.; Cao, Y.; Peng, Y.; Zeng, Z.; Nakanishi, Y.; Zhou, Y. Distributed Operation for Integrated Electricity and Heat System with Hybrid Stochastic/Robust Optimization. *Int. J. Electr. Power Energy Syst.* **2021**, *128*, 106680. [CrossRef]
14. Jamalzadeh, F.; Hajiseyed Mirzahosseini, A.; Faghihi, F.; Panahi, M. Optimal Operation of Energy Hub System Using Hybrid Stochastic-Interval Optimization Approach. *Sustain. Cities Soc.* **2020**, *54*, 101998. [CrossRef]
15. Correa-Posada, C.M.; Sanchez-Martin, P. Security-Constrained Optimal Power and Natural-Gas Flow. *IEEE Trans. Power Syst.* **2014**, *29*, 1780–1787. [CrossRef]
16. Correa-Posada, C.M.; Sanchez-Martin, P. Integrated Power and Natural Gas Model for Energy Adequacy in Short-Term Operation. *IEEE Trans. Power Syst.* **2015**, *30*, 3347–3355. [CrossRef]
17. Correa-Posada, C.M.; Sanchez-Martin, P.; Lumbreras, S. Security-Constrained Model for Integrated Power and Natural-Gas System. *J. Mod. Power Syst. Clean Energy* **2017**, *5*, 326–336. [CrossRef]
18. Cao, Y.; Xu, Y. Secure Operation of a Multi-Energy System: A Comprehensive Review. *Renew. Sustain. Energy Rev.* **2025**, *211*, 115312. [CrossRef]
19. Monie, S.W.; Gustafsson, M.; Önnered, S.; Guruvita, K. Renewable and Integrated Energy System Resilience—A Review and Generic Resilience Index. *Renew. Sustain. Energy Rev.* **2025**, *215*, 115554. [CrossRef]
20. Wang, J.; Shahidehpour, M.; Li, Z. Security-Constrained Unit Commitment with Volatile Wind Power Generation. *IEEE Trans. Power Syst.* **2008**, *23*, 1319–1327. [CrossRef]
21. Liu, C.; Shahidehpour, M.; Fu, Y.; Li, Z. Security-Constrained Unit Commitment with Natural Gas Transmission Constraints. *IEEE Trans. Power Syst.* **2009**, *24*, 1523–1536. [CrossRef]
22. Bertsimas, D.; Litvinov, E.; Sun, X.A.; Zhao, J.; Zheng, T. Adaptive Robust Optimization for the Security Constrained Unit Commitment Problem. *IEEE Trans. Power Syst.* **2013**, *28*, 52–63. [CrossRef]
23. Grigg, C.; Wong, P.; Albrecht, P.; Allan, R.; Bhavaraju, M.; Billinton, R.; Chen, Q.; Fong, C.; Haddad, S.; Kuruganty, S.; et al. The IEEE Reliability Test System-1996. A Report Prepared by the Reliability Test System Task Force of the Application of Probability Methods Subcommittee. *IEEE Trans. Power Syst.* **1999**, *14*, 1010–1020. [CrossRef]
24. Panteli, M.; Mancarella, P. Modeling and Evaluating the Resilience of Critical Electrical Power Infrastructure to Extreme Weather Events. *IEEE Syst. J.* **2017**, *11*, 1733–1742. [CrossRef]
25. Panteli, M.; Pickering, C.; Wilkinson, S.; Dawson, R.; Mancarella, P. Power System Resilience to Extreme Weather: Fragility Modeling, Probabilistic Impact Assessment, and Adaptation Measures. *IEEE Trans. Power Syst.* **2017**, *32*, 3747–3757. [CrossRef]
26. Artzner, P.; Delbaen, F.; Eber, J.M.; Heath, D. Coherent Measures of Risk. *Math. Financ.* **1999**, *9*, 203–228. [CrossRef]
27. Rockafellar, R.T.; Uryasev, S. Optimization of Conditional Value-at-Risk. *J. Risk* **2000**, *2*, 21–41. [CrossRef]
28. Rockafellar, R.T.; Uryasev, S. Conditional Value-at-Risk for General Loss Distributions. *J. Bank. Financ.* **2002**, *26*, 1443–1471. [CrossRef]
29. Zhu, J.; Li, G.; Guo, Y.; Chen, J.; Liu, H.; Luo, Y.; Liu, W. Real-Time Risk-Averse Dispatch of an Integrated Electricity and Natural Gas System via Conditional Value-at-Risk-Based Lookup-Table Approximate Dynamic Programming. *Prot. Control Mod. Power Syst.* **2024**, *9*, 47–60. [CrossRef]
30. Nemirovski, A.; Shapiro, A. Convex Approximations of Chance Constrained Programs. *SIAM J. Optim.* **2007**, *17*, 969–996. [CrossRef]
31. Calafiore, G.C.; El Ghaoui, L. On Distributionally Robust Chance-Constrained Linear Programs. *J. Optim. Theory Appl.* **2006**, *130*, 1–22. [CrossRef]
32. Delage, E.; Ye, Y. Distributionally Robust Optimization Under Moment Uncertainty with Application to Data-Driven Problems. *Oper. Res.* **2010**, *58*, 595–612. [CrossRef]
33. Zymler, S.; Kuhn, D.; Rustem, B. Distributionally Robust Joint Chance Constraints with Second-Order Moment Information. *Math. Program.* **2013**, *137*, 167–198. [CrossRef]
34. Cheng, J.; Chen, R.L.Y.; Najm, H.N.; Pinar, A.; Safta, C.; Watson, J.P. Chance-Constrained Economic Dispatch with Renewable Energy and Storage. *Comput. Optim. Appl.* **2018**, *70*, 479–502. [CrossRef]

35. Yang, Y.; Wu, W.; Wang, B.; Li, M. Chance-Constrained Economic Dispatch Considering Curtailment Strategy of Renewable Energy. *IEEE Trans. Power Syst.* **2021**, *36*, 5792–5802. [CrossRef]
36. Pan, D.; Zhang, L.; Wang, B.; Jia, J.; Song, Z.; Zhang, X. Multi-Objective Planning of Integrated Energy System Based on CVaR under Carbon Trading Mechanism. *Front. Energy Res.* **2024**, *12*, 1310301. [CrossRef]
37. Ji, D.; Wei, Z.; Zhou, Y.; Chen, S. Distributionally Robust Co-Optimization of Energy and Reserve Dispatch for Integrated Electricity-Gas-Heating Systems. *Sustain. Energy Technol. Assess.* **2025**, *73*, 104125. [CrossRef]
38. Parisio, A.; Rikos, E.; Glielmo, L. A Model Predictive Control Approach to Microgrid Operation Optimization. *IEEE Trans. Control Syst. Technol.* **2014**, *22*, 1813–1827. [CrossRef]
39. Bai, J.; Wei, W.; Chen, L.; Mei, S. Rolling-Horizon Dispatch of Advanced Adiabatic Compressed Air Energy Storage Based Energy Hub via Data-Driven Stochastic Dynamic Programming. *Energy Convers. Manag.* **2021**, *243*, 114322. [CrossRef]
40. Shen, W.; Zeng, B.; Zeng, M. Multi-Timescale Rolling Optimization Dispatch Method for Integrated Energy System with Hybrid Energy Storage System. *Energy* **2023**, *283*, 129006. [CrossRef]
41. Bødal, E.F.; Botterud, A.; Korpas, M. Capacity Expansion Planning with Stochastic Rolling Horizon Dispatch. *Electr. Power Syst. Res.* **2022**, *205*, 107729. [CrossRef]
42. Caramanis, M.C.; Bohn, R.E.; Schweppe, F.C. Optimal Spot Pricing: Practice and Theory. *IEEE Trans. Power Appar. Syst.* **1982**, *PAS-101*, 3234–3245. [CrossRef]
43. Schweppe, F.C.; Caramanis, M.C.; Tabors, R.D.; Bohn, R.E. *Spot Pricing of Electricity*; Kluwer Academic Publishers: Dordrecht, The Netherlands, 1988. [CrossRef]
44. Hogan, W.W. Contract Networks for Electric Power Transmission. *J. Regul. Econ.* **1992**, *4*, 211–242. [CrossRef]

Disclaimer/Publisher's Note: The statements, opinions and data contained in all publications are solely those of the individual author(s) and contributor(s) and not of MDPI and/or the editor(s). MDPI and/or the editor(s) disclaim responsibility for any injury to people or property resulting from any ideas, methods, instructions or products referred to in the content.